

Numerical investigation of the flat band Bloch modes in a 2D photonic crystal with Dirac cones

Peng Zhang,¹ Chris Fietz,¹ Philippe Tassin,²
Thomas Koschny,¹ and Costas M. Soukoulis^{1,3,*}

¹Ames Laboratory—U.S. DOE and Department of Physics and Astronomy,
Iowa State University, Ames, Iowa 50011, USA

²Department of Applied Physics, Chalmers University, SE-412 96, Göteborg, Sweden

³Institute of Electronic Structure (IESL), FORTH, 71110 Heraklion, Crete, Greece

*soukoulis@ameslab.gov

Abstract: A numerical method combining complex-k band calculations and absorbing boundary conditions for Bloch waves is presented. We use this method to study photonic crystals with Dirac cones. We demonstrate that the photonic crystal behaves as a zero-index medium when excited at normal incidence, but that the zero-index behavior is lost at oblique incidence due to excitation of modes on the flat band. We also investigate the formation of monomodal and multimodal cavity resonances inside the photonic crystals, and the physical origins of their different line-shape features.

© 2015 Optical Society of America

OCIS codes: (050.1755) Computational electromagnetic methods; (050.5298) Photonic crystals; (160.3918) Metamaterials.

References and links

1. J. D. Joannopoulos, R. D. Meade, and J. N. Winn, *Photonic Crystals: Molding the Flow of Light*, 2nd Edition (Princeton University Press, 2008).
2. P. Markos and C. M. Soukoulis, *Wave Propagation: From Electrons to Photonic Crystals and Left-Handed Materials* (Princeton University Press, 2008).
3. C. T. Chan, S. Datta, K. M. Ho, and C. M. Soukoulis, "A7 structure: A family of photonic crystals," *Phys. Rev. B* **50**, 1988–1991 (1994).
4. R. Moussa, S. Foteinopoulou, L. Zhang, G. Tuttle, K. Guven, E. Ozbay, and C. M. Soukoulis, "Negative refraction and superlens behavior in a two-dimensional photonic crystal," *Phys. Rev. B* **71**, 085106 (2005).
5. S. Foteinopoulou, E. N. Economou, and C. M. Soukoulis, "Refraction in media with a negative refractive index," *Phys. Rev. Lett.* **90**, 107402 (2003).
6. M. Diem, T. Koschny, and C. M. Soukoulis, "Transmission in the vicinity of the Dirac point in hexagonal photonic crystals," *Physica B* **405**, 2990–2995 (2010).
7. X. Huang, Y. Lai, Z. Hang, H. Zheng, and C. T. Chan, "Dirac cones induced by accidental degeneracy in photonic crystals and zero-refractive-index materials," *Nature Mater.* **10**, 582–586 (2011).
8. F. D. M. Haldane and S. Raghu, "Possible Realization of Directional Optical Waveguides in Photonic Crystals with Broken Time-Reversal Symmetry," *Phys. Rev. Lett.* **100**, 013904 (2008).
9. T. Ochiai and M. Onoda, "Photonic analog of graphene model and its extension: Dirac cone, symmetry, and edge states," *Phys. Rev. B* **80**, 155103 (2009).
10. X. Zhang, "Observing Zitterbewegung for Photons near the Dirac point of a Two-Dimensional Photonic Crystal," *Phys. Rev. Lett.* **100**, 113903 (2008).
11. K. Sakoda, "Dirac cone in two- and three-dimensional metamaterials," *Opt. Express* **20**, 3898–3917 (2012).
12. K. Sakoda, *Optical Properties of Photonic Crystals*, 2nd Edition (Springer, 2004).
13. M. Davanco, Y. Urzhumov, and G. Shvets, "The complex Bloch bands of a 2D plasmonic crystal displaying isotropic negative refraction," *Opt. Express* **15**, 9681–9691 (2007).

14. C. Fietz, Y. Urzhumov, and G. Shvets, "Complex k band diagrams of 3D metamaterial/photonic crystals," *Opt. Express* **19**, 19027–19041 (2011).
15. M. Jin, *The Finite Element Method in Electromagnetics*, 2nd Edition (Wiley, 2002).
16. S. G. Johnson, P. Bienstman, M. A. Skorobogatiy, M. Ibanescu, E. Lidorikis, and J. D. Joannopoulos, "Adiabatic theorem and continuous coupled-mode theory for efficient taper transitions in photonic crystals," *Phys. Rev. E* **66**, 066608 (2002).
17. M. Skorobogatiy, M. Ibanescu, S. G. Johnson, O. Weisberg, T. D. Engeness, M. Soljacic, S. A. Jacobs, and Y. Fink, "Analysis of general geometric scaling perturbations in a transmitting waveguide: fundamental connection between polarization-mode dispersion and group-velocity dispersion," *J. Opt. Soc. Am. B* **19**, 2867–2875 (2002).
18. C. Fietz, "Absorbing boundary condition for Bloch-Floquet eigenmodes," *J. Opt. Soc. Am. B* **30**, 2615–2620 (2013).
19. U. Fano, "Effects of configuration interaction on intensities and phase shifts," *Phys. Rev.* **124**, 1866–1878 (1961).

1. Introduction

Photonic crystals (PhCs), known as the semiconductors of electromagnetic waves, have been shown to exhibit a variety of novel properties and promising applications [1-5]. Recently, PhCs with Dirac cones have attracted widespread interest [6-11]. In 2011, X. Huang *et al.* [7] proposed a PhC structure with a square lattice. By modulating the lattice parameters, they found Dirac cones at the center of the Brillouin zone and, at the Dirac point, the PhC behaves similarly to a zero-index material. However, due to the symmetry of the lattice, a flat band crossing the Dirac point corresponding to magnetic longitudinal modes inevitably appears, and it is known that off-normal incident waves can excite modes from this flat band.

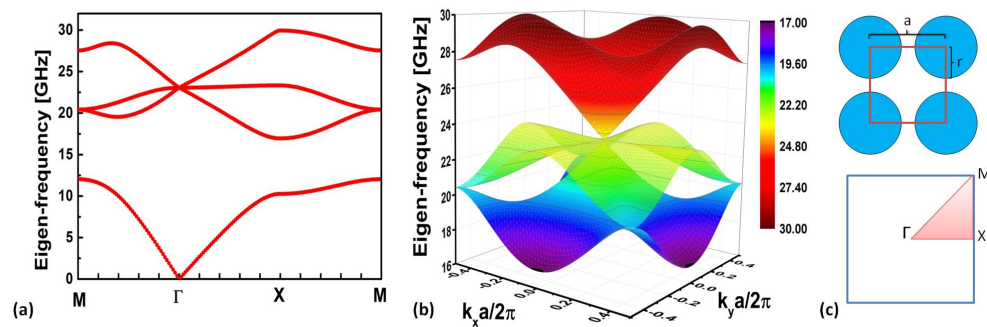


Fig. 1. (a) The band structure for TM modes (electric field parallel to the rod axis). There is a triple degeneracy at the Γ point and the Dirac frequency is 23.05161 GHz. (b) The full band structure in the 1st Brillouin zone. (c) The real lattice and its reciprocal lattice of the PhC. The embedded rods are made of alumina, with $\epsilon = 9.8$, $\mu = 1$. The radius of the cylinder is $r = 1.59$ mm, and the lattice constant is $a = 4.66153r$.

The purpose of this paper is to have a thorough study on the flat band Bloch modes using a newly developed method. Traditional methods employed for the study of PhCs include band calculations and reflection/transmission spectra measurements [12]. However, band calculations only give information on the number of Bloch modes and on the field structure of the modes. Scattering measurements give the macroscopic properties of a finite PhC while missing information on the details of the Bloch modes, such as how different modes interact and how each mode gets coupled into the radiated waves. In this paper, we resolve these shortcomings based on a new computational technique implemented in the commercial electromagnetics package COMSOL Multiphysics. In Section 2, we give an overview of the PhC under investigation, its Dirac cones, and its flat band. In Section 3, we calculate the complex-k band of

such a PhC and we demonstrate numerically how the flat band contributes to the behavior of the PhC, resulting in deviations from the the zero-index medium response when illuminated by a wave with a non-zero k_y (wave vector component parallel to the interface). In Section 4, by importing the numerical fields calculated in Section 3 and showing how to perfectly excite and absorb Bloch waves in the simulations, we study how the flat band modes couple and contribute to the transmission spectrum features using a semi-analytical formulation. We also have a brief discussion on the origin of the different line-shape features of the resonances and how the losses affect them.

2. 2D photonic crystals with Dirac cones

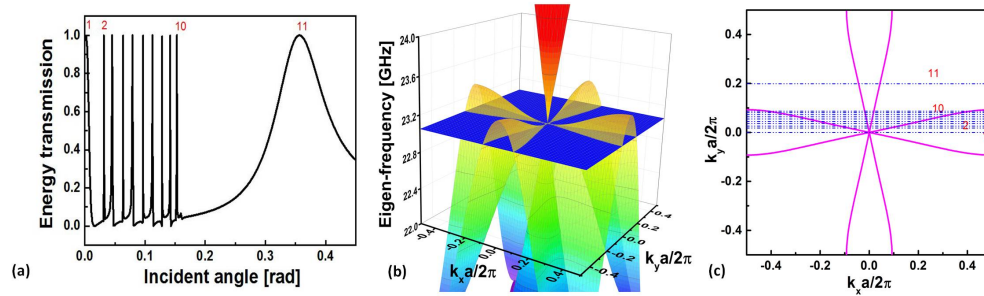


Fig. 2. (a) The transmission spectrum versus the incident angle. The PhC is finite in the propagation direction (x direction), in which 11 rows are present (refer to Fig. 4 for a visual sketch). (b) A cut-plane of the Dirac frequency over the full band. There are intersections with the middle band. (c) A top view of the cut-plane and the intersections. Each blue horizontal straight dash line indicates a certain k_y (component of the wave vector parallel to the interface between the air and PhC), or the incident angle. Numbers of the horizontal straight lines correspond to peaks in (a). It is shown that peak 1 corresponds to the zero-index mode with $k_x = k_y = 0$, due to the coupling with the linear branch. Peak 2 to 10 indicate there are 2 propagating modes with their reflective counterparts in the PhC, while peak 11 corresponds to only 1 propagating mode and its reflective counterpart, both due to the coupling with the flat band.

We present a detailed numerical study of the PhC with Dirac cones [7]. In our simulations, we took a square lattice in which alumina rods are periodically surrounded by vacuum. The permittivity and permeability of the alumina rods are chosen as 9.8 and 1, respectively. To reach the critical requirement on the geometrical parameters to obtain the accidental degeneracy, we set $a = 4.66153r$. This structure has a Dirac cone at the Γ point of its reciprocal lattice, i.e., at the center of the Brillouin zone. The band diagram showing the Dirac cone is plotted in Fig. 1.

However, as indicated in the supplementary material of [7], the flat band between the two cones is a longitudinal mode. Thus the PhC no longer has an effective zero-index when modes from this band are excited. This can be shown by calculating the transmission spectrum. When the electromagnetic waves are incident from air to an impedance-matched homogeneous dielectric slab with $\epsilon = \mu \rightarrow 0$, all electromagnetic waves are reflected except at normal incidence, which can be straightforwardly derived from the Fresnel equation. However, in our PhC, electromagnetic waves are still allowed to transmit at oblique incidence. Furthermore, the angular transmission spectrum of the PhC has Fabry-Perot-like features [see Fig. 2(a)]. This indicates that modes with a non-zero k_y have been excited. In the following sections, we present the results from our numerical investigation on these modes and we explore how these resonances are formed.

3. Complex-k band diagram and eigen-wavevector calculation

Generally, the eigenfrequencies of a PhC are calculated at given Bloch vectors, just as we did in Section 2. However, there are many cases in which knowing the eigenvalues of wave vectors at a given frequency is more helpful to study a photonic structure [13,14]. In our case, we are interested in how the modes look like and how they interact in the PhC at a given frequency (the Dirac frequency) and at a given incident angle. We now show that this information can be obtained from simulations with the package COMSOL Multiphysics, by specifying the field equations in their weak form.

In view of the Bloch theorem, the electric field in a periodic photonic structure can be written as the product of a periodic function and a plane wave envelope function:

$$\mathbf{E}(\mathbf{r}) = u(\mathbf{r})\exp(-i\mathbf{k} \cdot \mathbf{r})\hat{\mathbf{E}}, \quad u(\mathbf{r}) = u(\mathbf{r} + \mathbf{a}) \quad (1)$$

Taking the weak expression for TM waves (E field parallel to the rod axis) [13], we obtain:

$$\begin{aligned} 0 &= \int d\Omega \left[-\frac{k^2}{\mu} vu - \frac{iv}{\mu} \mathbf{k} \cdot \nabla u + \frac{i u}{\mu} (\nabla v) \cdot \mathbf{k} - (\nabla v) \cdot \frac{\nabla u}{\mu} + \frac{\varepsilon \omega^2}{c^2} vu \right] \\ &= \int d\Omega \cdot W \end{aligned} \quad (2)$$

where v is the test function of u . Since we only consider the in-plane (xy plane) wave vector, there are three degrees of freedom in the weak expression, k_x , k_y and ω , where k_y and ω are conserved over the air/PhC boundary. To calculate the eigenvalues of k_x , we need to prescribe the other two. We sweep the frequency within a large range containing the Dirac frequency for both normal ($k_y = 0$) and oblique ($k_y = 188 \text{ m}^{-1}$) incidence. Figure 3(a) and Fig. 3(b) show that, for the normal incidence, there is a triply degenerate point at $f = 23.05161 \text{ GHz}$ with eigenvalues $k_x = 0$ (black dots). Therefore, the Bloch wave is reduced to the periodic function $u(x, y)$, and the Bloch phase term turns into a constant independent of the propagation distance. Around the degeneracy point, the frequency is related linearly to the wave vector, as expected for a Dirac cone. However, the photonic crystal's behavior is quite different when we have a non-zero k_y . Figure 3(c) and Fig. 3(d) show that when $k_y = 188 \text{ m}^{-1}$, the Dirac cone and the zero-index mode disappear. Instead, more Bloch modes appear—the mode with vanishing $\text{Im}(k_y)$ is a propagating mode with propagation constant $k_x = 41.27 \text{ m}^{-1}$ (or 0.0487 in units of $2\pi/a$); the others with non-zero $\text{Im}(k_y)$ are attenuated modes.

4. Monomodal and multimodal resonances in the PhC slab

In the preceding sections, we analyzed the eigenmodes for a given frequency and one component of the wave vector, and we have concluded that when k_y is nonzero, there will be propagating Bloch modes inside the PhC. Therefore, these Bloch modes are likely to be reflected and transmitted multiple times at the interface between the PhC and air, just like the Fabry-Perot resonances for plane waves in a homogeneous dielectric slab. We hypothesize that this is the reason for the peaks appearing in the angular transmission spectrum. To prove this, we performed two sets of simulations. In one set, we measured the amplitudes and phases of both incoming and outgoing plane waves [Fig. 4(a)]. From $E_{\text{out}} = M_{\text{full}} E_{\text{in}}$, the transfer function M_{full} was calculated. In the other set, the transfer function under the assumption of multiple reflections should satisfy:

$$\begin{aligned} M_{\text{FP}} &= \mathbf{t}_{\text{pa}} \cdot \mathbf{A} \cdot \mathbf{t}_{\text{ap}} + \mathbf{t}_{\text{pa}} \cdot (\mathbf{A} \cdot \mathbf{r}_{\text{pa}} \cdot \mathbf{A} \cdot \mathbf{r}_{\text{pa}}) \cdot \mathbf{A} \cdot \mathbf{t}_{\text{ap}} + \mathbf{t}_{\text{pa}} \cdot (\mathbf{A} \cdot \mathbf{r}_{\text{pa}} \cdot \mathbf{A} \cdot \mathbf{r}_{\text{pa}})^2 \cdot \mathbf{A} \cdot \mathbf{t}_{\text{ap}} + \dots \\ &= \mathbf{t}_{\text{pa}} \cdot (\mathbf{I} - \mathbf{A} \cdot \mathbf{r}_{\text{pa}} \cdot \mathbf{A} \cdot \mathbf{r}_{\text{pa}})^{-1} \cdot \mathbf{A} \cdot \mathbf{t}_{\text{ap}} \end{aligned} \quad (3)$$

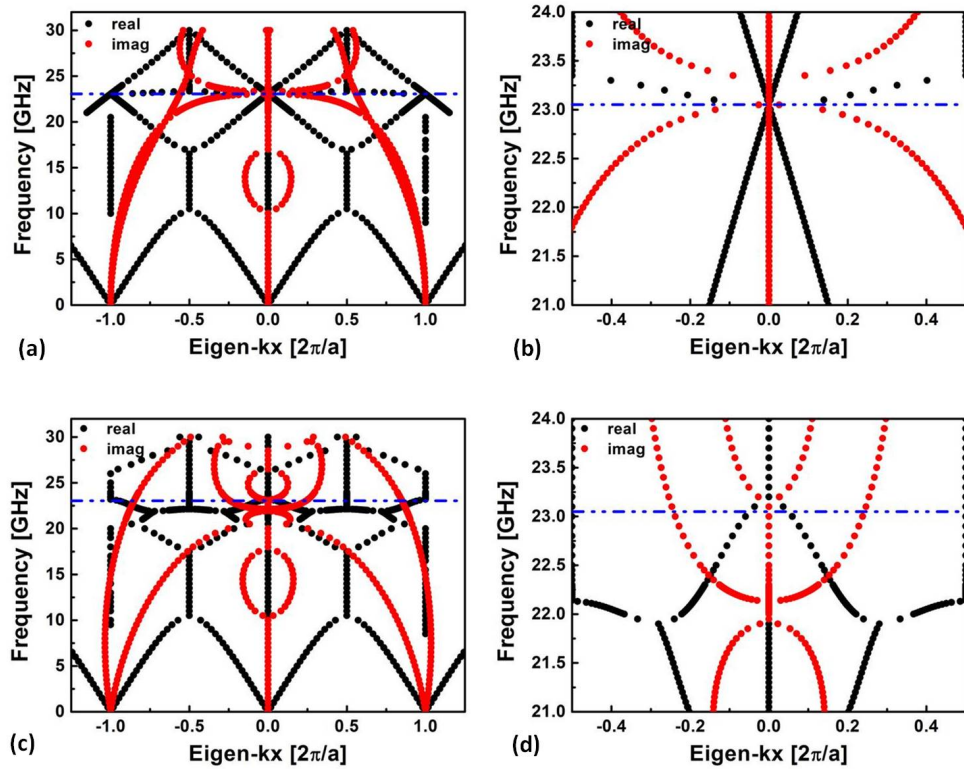


Fig. 3. Complex-k band diagram. x-axis: the eigenvalue of the propagating constant. y-axis: frequency of the EM wave. The black dots denote the real part of the eigen- k_x , and the red dots denote the imaginary part of the eigen- k_x . The blue dash shows where the Dirac frequency lies. (a)&(b): Complex-k band structure for normal incidence ($k_y = 0$) at different ranges of frequencies. (c)&(d): Complex-k band structure for the incident angle of 0.4 rad ($k_y = 188 \text{ m}^{-1}$) at different ranges of frequencies. From (a) and (c), we plot the extended Brillouin zone, from which we can see the periodicity for the real part of k_x .

The subscript “p” denotes PhC and “a” denotes air. \mathbf{t} and \mathbf{r} refer to the single-interface transmission and reflection coefficients at the interface between air and the PhC, and \mathbf{A} denotes the phase change of the Bloch mode when traveling from one end of the PhC to the other end. Generally, all variables in the equation should be a matrix, and the dimension of the matrix equals the number of the eigenmodes. Strictly speaking, the total field inside the PhC is a complete linear combination of all Bloch modes, including both propagating and evanescent modes. However, when the PhC waveguide is long enough, the effect of the evanescent modes can be neglected, and the resonant behavior is determined only by the propagating waves to a high degree of accuracy. Figure 1 shows the traditional band structure consisting of only the propagating modes. Figure 2(c) shows that peak 2 to 10 correspond to double propagating modes in the PhC, while peak 11 corresponds to a single propagating mode. In the monomodal case (peak 11), the matrix is reduced to a scalar, while in the bimodal cases (peak 2 to 10),

$$\mathbf{t}_{\text{ap}} = \begin{bmatrix} t_{\text{ap}}^1 \\ t_{\text{ap}}^2 \end{bmatrix} \quad \mathbf{r}_{\text{pa}} = \begin{bmatrix} r_{\text{pa}}^{11} & r_{\text{pa}}^{12} \\ r_{\text{pa}}^{21} & r_{\text{pa}}^{22} \end{bmatrix} \quad \mathbf{A} = \begin{bmatrix} \exp(-ik_{x1}x) & 0 \\ 0 & \exp(-ik_{x2}x) \end{bmatrix} \quad \mathbf{t}_{\text{pa}} = (t_{\text{pa}}^1 \quad t_{\text{pa}}^2) \quad (4)$$

The superscripts “1” and “2” denote different eigenmodes. The off-diagonal terms of the re-

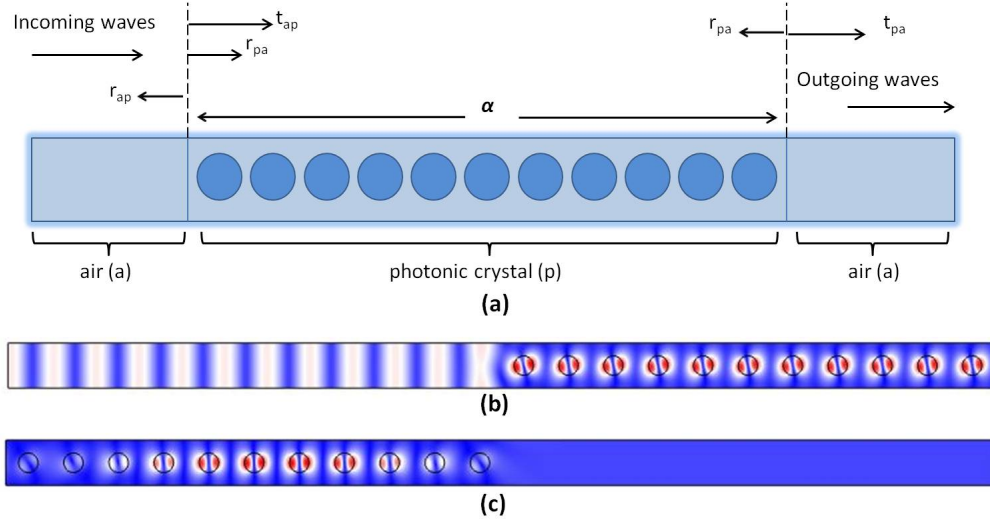


Fig. 4. (a) A sketch for multiple reflections in the PhC. The incoming and outgoing waves are plane waves. The field inside the PhC is the superposition of a set of Bloch waves. In the propagating direction (x direction), 11 rows of rods are present. In (b) and (c), $|E|$ is plotted, with $f = 23.05161$ GHz and $k_y = 188 \text{ m}^{-1}$. (b) Plane waves are excited and absorbed at the leftmost boundary, and the relevant Bloch modes are absorbed at the rightmost boundary. (c) One Bloch mode is excited and its reflective counterpart is absorbed at the leftmost boundary; plane waves are absorbed at the right.

flection matrix do not necessarily disappear, since there might be coupling between the two Bloch modes, or in other words, there might be transitions between different eigenmodes in the presence of a perturbation. Then the problem of measuring the transfer matrix turns into the problem of measuring the reflection and transmission coefficients at each interface. To resolve this, a port that can perfectly excite and absorb Bloch waves was developed. The port boundary condition is based on an orthogonality relation of the eigenmodes of the PhC. We again implement this via the weak form specification in the COMSOL package.

The weak expression for a general frequency domain EM problem can be separated into the domain and the boundary part [18], and the boundary term can be simplified as:

$$W_b = \mathbf{v} \cdot [\hat{\mathbf{n}} \times (\frac{1}{\mu} \nabla \times \mathbf{E})] = \pm i \frac{\omega}{c} v H_y \quad (5)$$

Here, we choose $\hat{\mathbf{n}} = -\hat{\mathbf{x}}$ at the input side (left) and $\hat{\mathbf{n}} = \hat{\mathbf{x}}$ at the output side (right). This constraint at the boundary allows us to define a port that can excite or absorb any mode, as long as we can expand it into a linear superposition of all known eigenmodes [(Eq. (11.1) in [15]], and retrieve each component by taking the inner product between the partial field and the total field, as long as a valid orthogonality relation is utilized. Note that, in a lossless system, we shall take Eq. (6) in [16] as the orthogonality relation, while in a lossy case, a generalized form is essential [Eq. (4) in [18]]. For a succinct summary, the field H_y of the Bloch modes that we need to excite or absorb reads

$$H_y = \sum_n |n\rangle \langle n| H_y \rangle = \sum_n h_{yn} \frac{\int dy (e_{zn}^* H_y + E_z h_{yn}^*)}{\int dy (e_{zn}^* h_{yn} + e_{zn} h_{yn}^*)}, \quad (6)$$

where e_{zn} and h_{yn} are the z component of the electric field and the y component of the magnetic field for the eigenmodes that we import from the calculations discussed in Section 2.

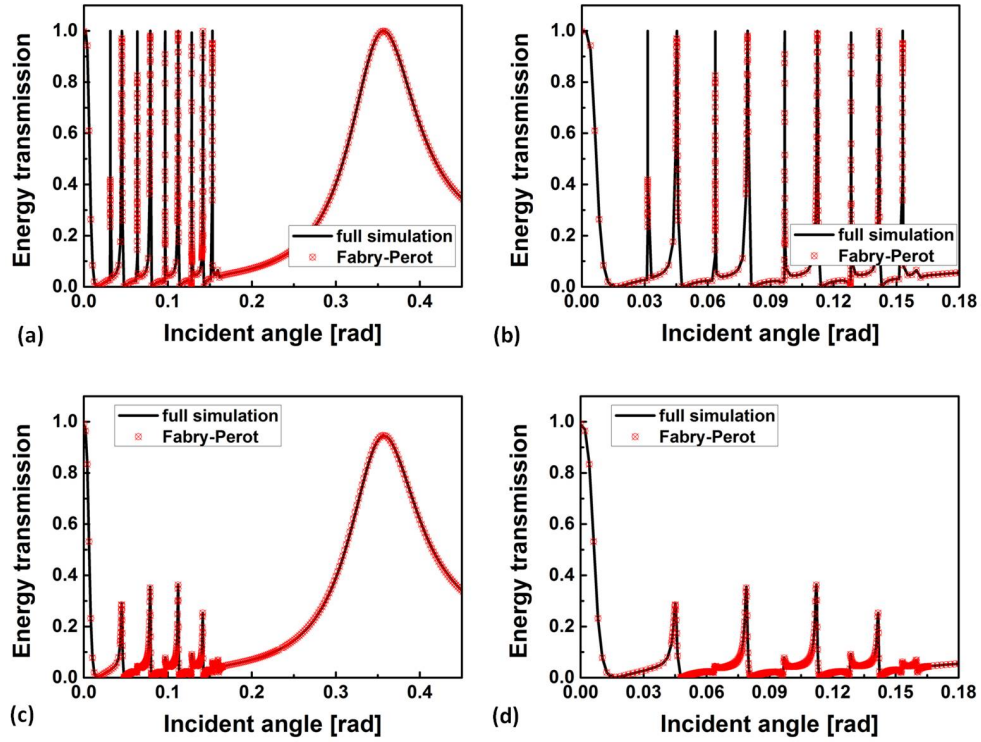


Fig. 5. Energy transmission($|M|^2$) vs. incident angle. The black lines denote the transfer function M which comes from the direct measurement of a full simulation in the air/PhC/air system. The red dots denote the transfer function M determined from the multiple reflection assumption. (a) and (b) correspond to a lossless system, where the alumina rods have $\epsilon = 9.8$. (c) and (d) correspond to a lossy system, where the alumina rods have $\epsilon = 9.8 + 6.8 \times 10^{-4}i$.

Figure 4 shows the setup. We truncate the air/PhC/air system into different sections. In Fig. 4(b), a plane wave with a given k_y is excited at the left and the corresponding Bloch wave is absorbed by the right port. From this simulation, we can determine t_{ap} . In Fig. 4(c), we import the eigenfield obtained from the complex- k band calculation in Section 3, and then this Bloch mode is excited and its reflective counterpart is absorbed. From the latter simulation, r_{pa} and t_{pa} can be obtained.

Figure 5(a) and Fig. 5(b) show a comparison between the energy transmission calculated from a full simulation and the multiple-scattering assumption. Both results are in excellent agreement, except for the smallest angles due to numerical precision limitations. Since the Q-factor is very high the spectrum contains some very narrow peaks for low incident angles which are difficult to resolve accurately numerically. By adding loss into the system (setting $\epsilon = 9.8 + 6.8 \times 10^{-4}i$ for the alumina rods), we effectively lower and broaden those peaks. In this way, results from both methods coincide perfectly in Fig. 5(c) and Fig. 5(d).

We can classify all these resonances into three categories. Peak 1 results from the excitation of an impedance-matched zero-index mode, which was the mode of interest in [7]. Peak 11 has a symmetric line shape, which is due to the multiple reflections and transmissions of a single Bloch mode in the PhC slab, and is the lowest-order resonance for the steep-slope mode

in Fig. 2(c). The other peaks at small incident angles are of more interest. Their asymmetric, or Fano-like, features indicate that at least two different modes contribute to the spectrum simultaneously, with one playing the discrete resonant role, and the other working as the continuous background process [19]. As a first-order approximation, we ignore the coupling (the off-diagonal term in r_{pa}) between those two eigenmodes, and we calculate the transfer matrix of each mode separately. Results are displayed in Fig. 6(a). The red resonant curve corresponds to the small-slope mode in Fig. 2(c). Its Fabry-Perot resonance origin preserves the symmetric line shape. The blue curve shows a continuous nonresonant feature, contributed by the steep-slope mode, and modifies the total transmission from symmetric to asymmetric. Since we did not consider the coupling term, the sum of each energy transmission does not add up to the real total. For a more rigorous analysis, one needs to take superpositions of the two eigen-Bloch modes to find the exact resonant and background modes, so that the coupling effects are taken into account. However, it's apparent that the small-slope mode dominates the bimodal resonance.

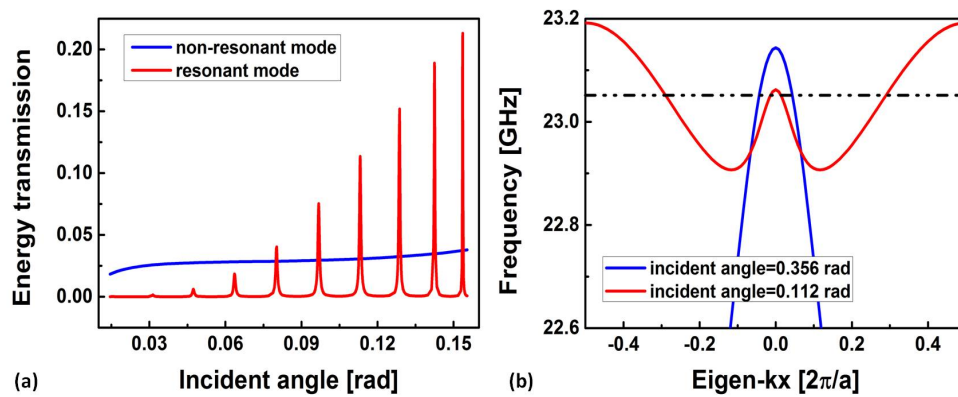


Fig. 6. (a) Energy transmission of both Bloch modes in the small incident angle regime, ignoring the coupling between them. The blue curve corresponds to the steep-slope mode in Fig. 2(c), while the red curve corresponds to the small-slope mode. (b) Dispersion relations of two excited modes with different incident angles. The black dashed-dot line marks the excitation frequency of 23.05161 GHz. Its intersection with the blue curve shows the propagating and counterpropagating Bloch waves excited at peak 11 in Fig. 2(a). The intersection with the red curve shows the two Bloch modes and their counterpropagating parts at small incident angle with respect to peak 7 in Fig. 2(a).

One might also have found that the small loss added into the system has a much more significant impact on the bi-modal resonance than the monomodal one, by suppressing the peak into less than half of its original. This can be understood from the dispersion relations. In Fig. 6(b), we plot the dispersion relations for two incident angles. The blue curve corresponds to the eigenmode with larger incident angle of 0.356 rad (peak 11), while the red curve corresponds to the bi-eigenmodes with smaller incident angle of 0.112 rad (peak 7). It is obvious that the resonant mode has a much smaller slope (group velocity) in the bimodal case than that in the monomodal case (approximately 2.7 times smaller in Fig. 6(b)). This slow light effect implies the existence of a higher density of states, making the field enhancement stronger and the Q-factor larger in a lossless system. However on the other side, these high Q-factor peaks will also be more sensitive to system losses, since a slower light is more readily absorbed when propagating.

In addition, since these peaks are the result of Fabry-Perot resonances, the number of the

peaks is related to the number of unit cells in the normal direction. As the slab grows thicker (the number of unit cells in the normal direction increases), the slab will be able to accommodate more resonant modes, and thus the number of sharp peaks will increase. The positions of the peaks will shift too. However, there is no one-to-one correspondence between the number of peaks and the number of unit cells. Recalling that the resonant wavelengths of a Fabry-Perot cavity are typically functions of the size of the cavity, i.e, for a perfect Fabry-Perot cavity, a strict standing wave boundary condition has to be met, a similar situation happens to the monomodal resonance at large incident angles. When there is only one propagating Bloch mode excited, the denominator of the the transfer matrix in Eq. (3) is commutable and reduces to $[1 - r_{\text{pa}}^2 \exp(-2jk_x d)]^{-1}$. Therefore the position of the monomodal resonance could be estimated as $k_x d \sim n\pi$, due to the non-zero phase at the boundary and on condition that no higher-order diffraction happens. In the bimodal case, the simulation becomes more complex, since there will be no simple standing-wave conditions. However, one can always find the resonant positions by performing a numerical study of the denominator as we have already shown.

5. Conclusion

In this paper, we reported on a numerical study of the flat band Bloch modes in a photonic crystal with Dirac cones. We proved numerically that the non-zero k_y gives rise to non-zero index medium behavior. Furthermore, to understand how modes propagate and interact in the PhCs, we derived the weak expressions and performed the complex-k band and transmission calculations. Though the explanation of the spectral features turns out to be multiple reflections of the eigenmodes, the simulation method offers us a way to separate the coupled Bloch modes in a PhC slab and manipulate each with great freedom. We use this method to explain the physical origins of the different line-shape features in the transmission spectrum. In addition, our method allows to study the surface scattering of a truncated PhC by eliminating the back reflection. We believe that our method of analysis will prove beneficial to understand the scattering properties of more complicated photonic crystal structure of final extent.

Acknowledgments

The work at Ames Laboratory was partially supported by the US Department of Energy, Office of Basic Energy Science, Division of Materials Sciences and Engineering (Ames Laboratory is operated for the US Department of Energy by Iowa State University under Contract No. DE-AC02-07CH11358) (simulations) and by the European Research Council under the ERC advanced Grant No. 320081 (PHOTOMETA) (theory) and the IC Postdoctoral Fellowship Program.